FLood2 Vortex Flood Fill Algorithm and Fourier Analysis for Turbulence Characterization of Single Phase Flow Through a Helical Coil

Samuel Harrison

Department of Chemical and Biological Engineering
University of Ottawa
Ottawa, Canada
sharr125@uottawa.ca

Abstract—**This work presents the development and application of a novel flood fill algorithm, FLood2, for turbulence characterization built on the Lambda 2 criterion. Direct numerical simulation (DNS) using the spectral element method (SEM) was used to simulate helical coil flow at Reynolds numbers of 50, 100, and 500. Fourier analysis revealed these that cases did not produce an adequate amount of turbulence, so the algorithm was instead validated using data from turbulent flow in a milli-structured serpentine channel. FLood2 analyzed vortex size distributions, quantity, and positions across multiple λ_2 thresholds, significantly extending the capability of the traditionally qualitative Lambda 2 criterion. Results demonstrated that an increase in Reynolds number led to smaller average vortex volumes due to fragmentation of large vortical structures and emergence of new small-scale structures. Likewise, an increase in Reynolds number flattened the lower λ_2 threshold volume distributions. Stricter thresholds increased average vortex size, matching the turbulent energy spectrum where most energy comes from low frequency large-scale eddies. Future work will involve applying FLood2 to higher Reynolds number simulations in helical coils, and using vortex location data in symmetrical geometries.**

Index Terms—**Vortex Detection, Turbulence Characterization, Helical Coil, Lambda2, Fourier Analysis**

I. Introduction

Helically coiled pipes are extensively used in engineering applications as they provide a more compact arrangement while significantly increasing fluid mixing and heat transfer when compared to straight pipes[1,2]. Practical applications of helical coils include heat exchangers, ultrafiltration systems, rectification and absorption columns, nanofluid transport, chemical reactors, nuclear reactors, and various piping systems, making them an important subject of research[3].

The primary physical mechanism responsible for greater mixing and heat transfer in helical coils is the formation of secondary flows structures known as Dean vortices. Dean vortices are the result of an imbalance between centrifugal and inertial forces acting on the fluid as it flows through a curved geometry. These vortices induce a twin counter-rotating vortex cross-sectional flow pattern that continuously transports fluid from the pipe center toward the wall[4].

The flow characteristics of Dean vortices are highly dependent on geometric parameters, fluid velocity, and fluid properties. Specifically, the vortices are characterized by the Dean number De, a dimensionless quantity defined as a function of the Reynolds number Re and the ratio between the coil pipe radius r_c and the coil turn radius R_t :

$$De = \frac{\rho D v}{\mu} \sqrt{\frac{r_p}{R_t}} = Re \sqrt{\frac{r_p}{R_t}} \qquad (1)$$

At low Dean numbers, typically below 60, the secondary flow is minimal, and the fluid behaves similarly to flow in a straight pipe. As the Dean number increases into the range of 75 to 200, the classic twin counter-rotating Dean vortices develop and stabilize the flow, increasing the critical Reynolds number and delaying the transition into the turbulent regime[5]. Dean numbers greater than this begin to generate secondary instabilities, before eventually developing into incoherent turbulence[6].

Flow through helical coils has been extensively investigated in the literature, across a large range of Reynolds numbers and geometric parameters[3,5,7,8]. However, these have largely been explored using finite volume methods (FVM) and finite element methods (FEM), and results have been primarily focused on pressure drops, friction factors, flow regime transitions, and velocity profiles. Direct numerical simulation (DNS) using the spectral element method (SEM) has been successfully been applied in other geometries to fully resolve vortices of all scales given its exponential convergence for smooth solutions[9]. This study applies DNS with SEM specifically to a helically coiled geometry to achieve similar objectives.

The Lambda 2 criterion (λ_2) remains one of the most popular vortex detection and visualization methods, in large part due to its robustness and computational simplicity[10,11]. However, it's nature is highly qualitative as it relies on an arbitrary value cutoff, limiting its effectiveness as a quantitative turbulence characterization method[12]. To address this shortcoming of an otherwise robust method, this work outlines the development and analysis of a flood fill algorithm designed to quantitatively track the number, sizes, and spatial locations of vortex structures across a range of λ_2 thresholds.

II. Geometry and Meshing

A. Helical Coil Geometry

As seen in Fig. 1, a helically coiled pipe can be uniquely specified by three geometric parameters; the diameter of the coils pipe, the turn diameter of the coil, and its pitch.
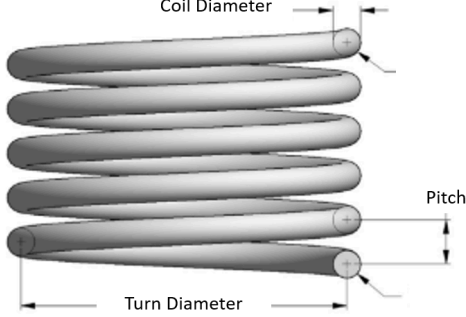

Fig. 1: Parameterization of a helical coil pipe into it's coil pipe diameter D_p, turn diameter D_t, and pitch p.

From these parameters, other geometric dimensionless groups can be derived, notably the curvature and torsion :

$$\delta = \frac{D_p}{D_t} \tag{2}$$

$$\lambda = \frac{p}{2\pi D_p} \tag{3}$$

An increase in the dimensionless curvature number results in stronger secondary vortices, so as the limit of the curvature approaches 0, the velocity profile becomes that of a straight pipe. Conversely, an increase in curvature results in a higher pressure drop and a more delayed transition to the turbulent regime. Higher torsion simply twists the twin Dean vortex plane further away from the radial line connecting the inner and outer walls, so the angle between that line and the vortex plane grows as torsion increases[13–16].

The coil dimensions selected for this numerical study were chosen based on an existing physical coil, and are summarized in Table I. Matching these will allow for a direct comparison with experimental results in future works.

TABLE I: Geometric parameters of the helical coil used in the present simulations.

Parameter	Size [mm]
Pipe Diameter, D_p	4.76
Turn Diameter, D_r	54.8
Pitch, p	5.95

These parameter are equally used to calculate the conversion ratio from Reynolds number to Dean number. For this specific geometry, the Dean number is 3.4 times smaller than the Reynolds number.

B. Mesh Generation

The mesh was generated using Gmsh, an open source 3D finite element mesh generator[17]. As seen in Fig. 2, the mesh is made up entirely of structured hexahedral elements, with biased edges on the pipe face to account for the steeper gradients that occur normal to the wall of the pipe. An octagonal O-grid was selected to reduce skew between cells at the transition from boundary layer cells to pipe center cells.
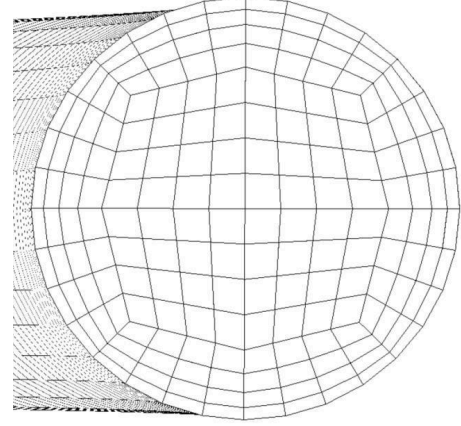

Fig. 2: Axial cross-section through the helical coil showing the structured hexahedral O-grid mesh with wall-normal boundary-layer refinement

As shown in Fig. 3, the computational domain spans two complete turns to eliminate entrance effects and ensure a fully developed flow, as this is the flow regime of interest. This choice was made based on previous work using a similar geometry which found that with a uniform inlet velocity the downstream flow pattern no longer changed past an azimuthal angle of $\varphi = 240°$[5]. To further accelerate profile development, a fully-developed laminar flow profile for a straight pipe was prescribed.
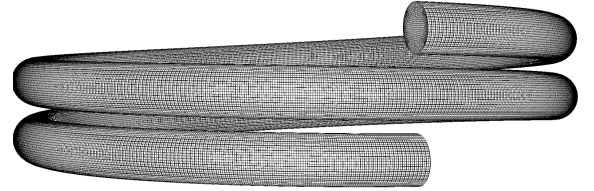

Fig. 3: Complete two-turn helical coil computational domain meshed with structured hexahedral elements.

Given the SEM uses high-order polynomial basis functions to approximate the solution within each element, the mesh used here is significantly coarser compared to meshes typically required by FEMs and FVMs.

C. p-type Refinement

Grid independence was assessed by performing p-type mesh refinement, in which the polynomial degree of the spectral elements are increased on a fixed hexahedral grid. The a priori error estimate yields a proportionality of :

$$E \propto h^{\min(r,p)} \tag{4}$$

where h denotes the element size, p the polynomial order, and r the regularity exponent of the exact solution. When the flow field is sufficiently smooth, p is larger than r and so the error proportionality becomes :

$$E \propto h^p \tag{5}$$

From this, it becomes clear that increasing p produces exponential convergence, whereas h-refinement alone achieves only algebraic convergence[18]. In the present helically coiled configuration with a smooth laminar inlet profile, it is safe to assume the solution regularity exceeds the maximum p used, meaning that p-type refinement attains spectral accuracy and produces a more reliable estimate of convergence since the bounded error decays exponentially[19]. P-type refinement was preferred over hp-adaptation because of its simplicity and the ability to reuse the same mesh for all Reynolds number cases.

Convergence of the bulk flow was verified by monitoring the time-averaged viscous dissipation rate as a function of the polynomial order. Based on Table II, the dissipation rate exhibited negligible variation cross quadrature modes $p = 3 - 5$, confirming that the flow field is fully resolved using only 3 modes.

TABLE II: Time-averaged viscous dissipation rates at Reynolds numbers $Re = 50, 100, 500$ for polynomial orders $p = 3-5$, and their percent change from the previous quadrature modes.

Reynolds Number	Quadrature Modes	Viscous Dissipation	Change
50	3	N/A	-
	4	N/A	N/A%
	5	N/A	N/A%
100	3	3.498e-3	-
	4	3.504e-3	0.17%
	5	N/A	N/A%
500	3	1.339e-01	-
	4	1.340e-01	0.07%
	5	1.338e-01	0.15%

Boundary-layer resolution was quantified via the dimensionless wall distance y^+ :

$$y^+ = \frac{y u_\tau}{\nu} \tag{6}$$

where y is the distance from the wall to the first quadrature point, ν the kinematic viscosity, and u_τ the friction velocity defined by

$$u_\tau = \sqrt{\frac{\tau_w}{\rho}} \tag{7}$$

with wall shear stress

$$\tau_w = \rho \nu \left(\frac{d<U>}{dy} \right)_{y=0} \tag{8}$$

The quadrature point distances normal to the wall required by (6) are tabulated in Table III for the quadrature modes used.

TABLE III: Distance from the wall to the first quadrature point for each quadrature mode.

Quadrature Mode	Distance
3	$\frac{1}{2}\sqrt{\frac{3}{5}}$
4	$\frac{1}{2}\sqrt{\frac{3}{7} - \frac{2}{7}\sqrt{\frac{6}{5}}}$
5	$\frac{1}{6}\sqrt{5 - 2\sqrt{\frac{10}{7}}}$

Wall shear was extracted using a post-processing utility, and the maximum value was used to compute y^+. The resulting y^+ values in Table IV confirm that the near-wall region is adequately resolved for all simulation cases with only 3 quadrature modes. **This section might require change in the very unlikely event that the y+ values come back and indicate that higher modes are needed**.

TABLE IV: Maximum dimensionless wall distance y^+ for each Reynolds number and polynomial order

Reynolds Number	Quadrature Modes	y^+	Change
50	3	N/A	-
	4	N/A	N/A%
	5	N/A	N/A%
100	3	N/A	-
	4	N/A	N/A%
	5	N/A	N/A%
500	3	N/A	-
	4	N/A	N/A%
	5	N/A	N/A%

III. Simulation Setup

A. Nektar++ Spectral Element Method

Simulations were carried out with Nektar++, an open-source spectral/hp element solver for the incompressible Navier–Stokes equations[20]. The solver settings from the cases are summarized in Table V. An implicit-explicit second-order backward differentiation formula time integration scheme was used, treating nonlinear convection explicitly to avoid expensive iterative solves and diffusion implicitly for a larger time step. The standard velocity correction scheme was selected for the solver.

Gradient-jump penalty (GJP) stabilization was added to help stabilize potentially under resolved simulations and reduce oscillations between elemental boundaries. The GJP scaling parameter is set using the number of pressure quadrature modes; the specific heuristic chosen was based on a regression across the range of polynomial orders used[21].

PDE aliasing can arise in simulations containing non-linear terms, and geometric aliasing from curved geometries or elements. Dealiasing strategies have proven themselves very effective in enhancing the numerical stability of SEM simulations. By increasing the number of quadrature points while keeping the number of modes the same, energy in shorter

length scales can be properly resolved without a large runtime penalty[22–25].

The time step was configured to target a CFL value of 0.2, keeping the simulation stable and the results time-accurate.

TABLE V: Nektar++ solver settings for the simulation of flow through a helical coil.

Setting	Value
SolverType	VelocityCorrectionScheme
TimeIntegrationMethod	IMEXGear
GJPJumpScale	$0.8(P+1)^{-4}$
NUM_POINTS	$\frac{3}{2}$NUM_MODES
TimeStep	$\Delta t \mid \text{CFL} \leftarrow 0.2$

The boundary conditions of the problem are summarized in Table VI. At the inlet, the velocity components in the face's plane, u and w, are set to zero, while the normal component v follows a parabolic laminar profile offset in the y-direction by one coil-turn radius and centered in z. No-slip conditions on the pipe walls and homogeneous Neumann conditions at the outlet are applied for the velocity fields. The pressure field is subject to homogeneous Neumann conditions at the inlet and walls, and a zero-valued Dirichlet condition at the outlet.

TABLE VI: Boundary conditions for the simulation of flow through a helical coil.

Field	Inlet	Walls	Outlet
u	0	0	$\partial u \partial n = 0$
v	$-2 * v * \left(1 - \left(\frac{r}{R_t}\right)^2\right)$	0	$\partial v \partial n = 0$
w	0	0	$\partial w \partial n = 0$
p	$\partial P \partial n = 0$	$\partial P \partial n = 0$	0

B. Simulation Cases and Execution

As shown in Table VII, three flow cases were simulated at Reynolds numbers of 50, 100, and 500, corresponding to Dean numbers of 14.7, 29.5, and 147.4, to cover regimes from nearly straight-pipe behavior through the onset and full development of Dean vortices. Each case proceeded through three sequential phases where the solution was first advanced for a short time at a low CFL of 0.01 to establish a stable initial field. Next, the flow was developed over one residence time at the target CFL of 0.2. Finally, an additional residence time under identical conditions was simulated to collect the time-averaged and instantaneous flow data.

TABLE VII: Nektar++ cases for the simulation for the simulation of flow through a helical coil.

Case [-]	Reynolds Number [-]	Dean Number [-]	Max Inlet Velocity [m/s]
1	50	14.7	9.37e-3
2	100	29.5	1.88e-2
3	500	147.4	9.37e-2

To collect data for the temporal Fourier analysis, instantaneous velocity field values were collected at various points in the pipe cross-section, shown in Fig. 4. The data points were recorded one half-turn upstream of the outlet such that the flow was fully developed at the sampling plane, and at a frequency of once every 10 time steps to capture high frequency modes.
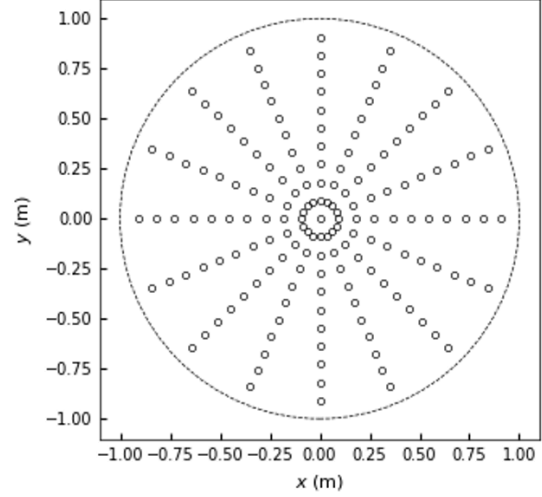

Fig. 4: Fourier analysis sampling point locations on pipe cross section $\frac{1}{2}$ turn upstream from the outlet.

IV. FLood2 : Turbulence Characterization

A. L_2 Criterion Background

Identification and subsequently visualization of vortical structures is fundamental for characterizing coherent motions within complex flows[26].

Most detection methods are based on the velocity-gradient tensor, J, including the Lambda 2 method, which is the backbone of the algorithm being developed in this section.

$$J \equiv \nabla\vec{u} = \begin{bmatrix} \frac{\partial u}{\partial x} & \frac{\partial u}{\partial y} & \frac{\partial u}{\partial z} \\ \frac{\partial v}{\partial x} & \frac{\partial v}{\partial y} & \frac{\partial v}{\partial z} \\ \frac{\partial w}{\partial x} & \frac{\partial w}{\partial y} & \frac{\partial w}{\partial z} \end{bmatrix} \quad (9)$$

This transformation matrix can uniquely decomposed into two physically distinct components: a symmetric strain-rate tensor, S, and an antisymmetric rotation-rate tensor, Ω.

$$S = \frac{J + J^\top}{2} \quad (10)$$

$$\Omega = \frac{J - J^\top}{2} \quad (11)$$

Physically, the symmetric strain-rate tensor represents fluid deformation associated with stretching and compression without rotation, whereas the antisymmetric rotation-rate tensor represents the pure rotational motion of the fluid.

Under the assumptions of incompressibility, negligible viscous effects, and negligible irrotational straining, the Navier–Stokes equations simplify in a way as to allow the second-order tensor combination $\Omega^2 + S^2$ to directly correlate with the existence of a local pressure minimum, which is a necessary but not sufficient condition for a vortex core[10].

$$\mathbf{\Omega}^2 + \mathbf{S}^2 = -\frac{1}{\rho}\nabla^2 P \qquad (12)$$

The symmetric strain tensor admits only real eigenvalues, and thus positive and real eigenvalues for the square. Conversely, the antisymmetric rotation tensor results in up to 2 imaginary eigenvalues, which become negative and real when squared. So, the combination of the squares of these two tensors results in a symmetric tensor whose eigenvalues signs are determined by whether the stress or rotation eigenvalues had the greater magnitude. By taking the eigenvalues and sorting them,

$$\left\{\lambda_{(1)}, \lambda_{(2)}, \lambda_{(3)}\right\} = \sigma\left(\mathbf{S}^2 + \mathbf{\Omega}^2\right) \qquad (13)$$

$$\lambda_{(1)} \le \lambda_{(2)} \le \lambda_{(3)}$$

the second eigenvalue $\lambda_{(2)}$ yields the λ_2 criterion used for vortex identification, which is the result of comparing the weaker strain value with the rotation.

The magnitude of the second most negative eigenvalue is directly proportional to the strength of rotation relative to strain; a more negative λ_2 signifies a stronger vortex structure. However, the practical implementation of the λ_2 criterion typically involves visualizing isocontours of it's scalar field. Determining the appropriate cutoff threshold for these contours is completely qualitative, and common methods to select this threshold include subjective visual inspection, or a fixed volume fraction of the fluid domain for comparing multiple flows[9,27]. Both approaches introduce substantial variability and limit the criterion's effectiveness in quantitative turbulence characterization or comparing trends across flows.

B. Algorithm Development and Analysis

To address the inherent subjectivity and limited quantitative capabilities of the conventional λ_2 method, a flood-fill-based vortex characterization algorithm termed FLood2 was developed. This algorithm evaluates vortex structures across a range of λ_2 threshold values, providing quantitative metrics such as vortex size, quantity, and location.

The FLood2 algorithm initially computes the λ_2 scalar field from the simulated velocity field using the standard λ_2 criterion. This scalar field is computed at mesh vertices using the Nektar++ λ_2 post-processing utility. To facilitate subsequent quantitative analysis, the values initially defined at mesh vertices are interpolated to cell centers by taking the arithmetic average of the λ_2 values at the cell's eight vertices.

Additionally, the quantitative analysis requires computation of the cell volumes. For fully structured hexahedral meshes, each hexahedral cell volume is calculated by decomposing the cell into a set of tetrahedra whose volumes are computed via the scalar triple product. Given the consistent vertex ordering guaranteed by the VTK standard, this decomposition and volume computation is straightforward and unambiguous.

The core of the FLood2 algorithm uses a breadth-first search (BFS) flood-fill. First, an adjacency map is created, identifying neighboring cells based on the number of shared vertices to allow for constant time lookup of neighbors. In structured hexahedral meshes, two cells are neighbors if and only if they share exactly four vertices.

For each λ_2 cutoff in the range, the BFS process explores contiguous cells whose λ_2 values lie below a specified threshold, marking each group of connected cells as a distinct "island" or vortex region. A simple strategy for selecting the range of threshold values will be detailed in Section V. For each identified island, the algorithm records quantitative properties such as the total volume occupied by the vortex and its volume-weighted centroid position. The pseudocode detailing this procedure for a single threshold is provided in Algorithm 1, where **A** is a cell adjacency map `HashMap<Cell, Cell>`, and **threshold** is the λ_2 `float` threshold for that iteration.

Algorithm 1: bfs(A, threshold)

```
1  visited ← set()
2  islands ← list()
3  for cell in A.keys():
4      if cell in visited or cell.L2 ≥ threshold:
5          continue
6      stack ← list(cell)
7      total_volume ← 0.0
8      cell_count ← 0
9      weighted_moment ← list(0,0,0)
10     while stack is not empty:
11         curr ← stack.pop()
12         if curr in visited:
13             continue
14         visited.add(curr)
15         if curr.L2 ≥ threshold:
16             continue
17         cell_count += 1
18         total_volume += curr.volume
19         weighted_moment += curr.volume * curr.centroid
20         for neighbor in A[curr]:
21             if neighbor not in visited:
22                 stack.push(neighbor)
23     islands.append({
24         volume: total_volume,
25         centroid: weighted_moment / total_volume
26     })
27 return islands
```

BFS is then run across the range of thresholds, as detailed in Algorithm 2, where `start` and `stop` are the bounding values for the λ_2 range, and `m` is the number of samples taken in that range.

Algorithm 2: FLood2(A, start, stop, m)

---

1   thresholds ← linspace(start, stop, m)

2   islands ← map()

3   **for** threshold **in** tresholds:

4 | islands[threshold] ← bfs(A, treshold)

5   **return** islands

Since FLood2 must examine every one of the n cells for each of the m sampled λ_2 thresholds, its overall computational cost scales as $\mathcal{O}(m*n)$, where n is the total cell count in the mesh and m is the number of threshold values investigated.

A significant advantage of the FLood2 algorithm is its inherent parallelizability. First, the m sampled thresholds can be trivially distributed, since each threshold's flood-fill is entirely independent from the others. Then, by using a mesh partitioning library such as Scotch or Metis, the domain for a given threshold can be subdivided into multiple non-over-lapping subdomains. A separate thread for each partition can independently execute the BFS from its set of seed cells, maintaining its own stack and *visited* set. To account for vortices straddling partition boundaries, islands are appended to a global hashset keyed by centroid, deduplicating any vortices. Given this, the algorithm can be added to any turbulence analysis without incurring a large runtime penalty.

V. Results

A. Unfortunate Lack of Turbulence

After running the previously described simulations and performing the Fourier analysis on the resulting velocity field history points, it became evident that the flows did not exhibit any turbulent characteristics. Consequently, there was no turbulence to quantify or characterize. This absence of turbulent behavior is particularly obvious when examining the the velocity magnitude over time in Fig. 5, which shows a steady velocity field devoid of any perturbations.
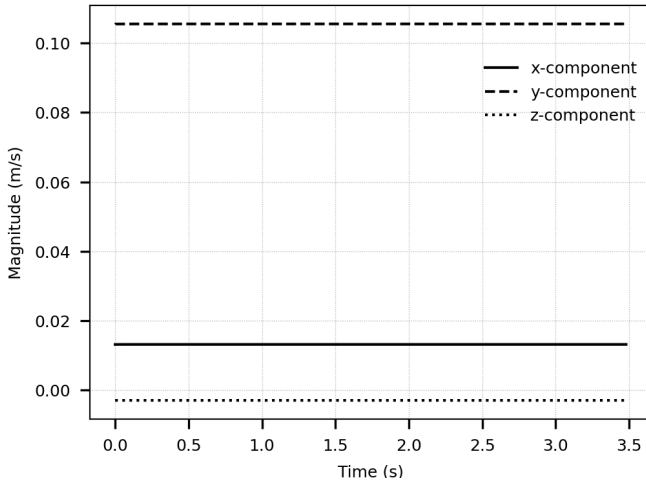

Fig. 5: Velocity magnitude over time at Re = 500.

Looking at Fig. 6's pipe cross-sectional velocity profiles at Reynolds numbers of 100 and 500, the centrifugal forces shift the velocity maxima towards the outer wall, and the quiver plot overlay shows the beginning of the formation of Dean vortices. At Re = 100 the profile remains essentially laminar with only slight skewness; at Re = 500 increased curvature and distortion appears near the outer boundary but the flow retains clearly laminar characteristics. In both cases, the secondary flow intensity is insufficient to induce transition to turbulence. Based on experimental correlations, turbulence would be expected at a Reynolds number of 9500 for a helical coil with a coil radius to turn radius ratio of 11.5[28].
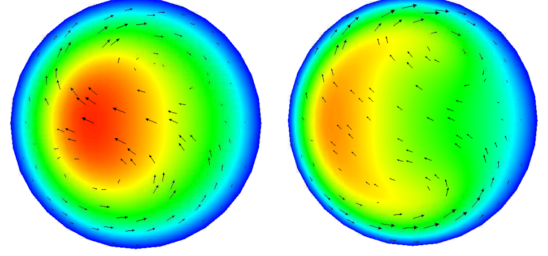

Fig. 6: Helically coiled pipe cross-sectional velocity magnitudes and vector fields at Re = 100 (left) and Re = 500 (right).

Applying the FLood2 algorithm to these flow fields resulted in the identification of only one continuous vortex region encompassing nearly the entire fluid domain, confirming the lack of discrete turbulent structures.

B. SZ Geometry Turbulent Flow Characterization

Due to the absence of turbulence in the helical coil simulations, an alternative geometrical configuration, the SZ geometry, was analyzed in a Reynolds number range where turbulent flow conditions were known to exist.

Based on the of the velocity magnitude contours of cross-sectional slices in Fig. 7, Reynolds numbers of 500 and 1000 create abundant turbulent structures, whose presence and intensity increase notably as the Reynolds number is elevated.
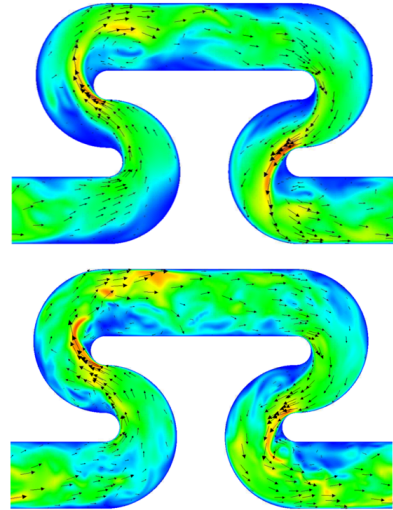

Fig. 7: SZ geometry cross-sectional velocity magnitudes and vector fields at Re = 500 (top) and Re = 1000 (bottom).

Likewise, after filtering out all positive λ_2 regions and examining the cross section contour plot of the log of the λ_2 criterion in Fig. 8, a distinct shift in the vortical structures can be seen, including significant changes in vortex sizes, distributions, and quantities.
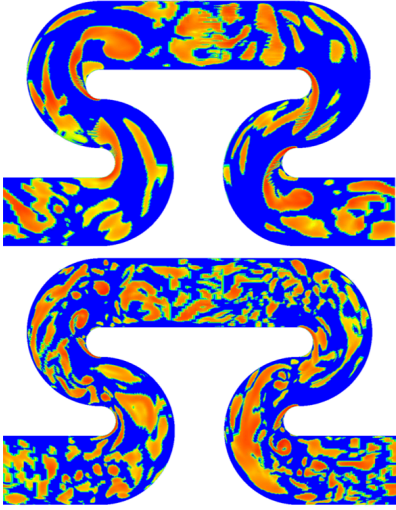

Fig. 8: SZ geometry cross-sectional of $\log_{10}(\max(1, -\lambda_2))$ at Re = 500 (top) and Re = 1000 (bottom).

C. Quantitative Analysis using FLood2 Algorithm

Initial distributions of volume-weighted λ_2 values offered limited insight as they spanned many orders of magnitude. However, once regions dominated by strain were excluded and the remaining values transformed using the logarithm of their absolute values, a clear log-normal distribution emerges, shown in Fig. 9. This demonstrates that higher Reynolds number flows produce stronger vortices, showing an approximately 20% increase in average vortex intensity on the log scale when doubling the inlet velocity. The skew in the distributions reflect the fact that large, high-energy eddies fragment into smaller structures more quickly than the reverse process, so very strong vortices are rarer, suppressing the upper tail. A slight reduction in standard deviation was also noted at Re = 1000, however, without additional data points the significance of this correlation remains inconclusive. Most importantly of all, these distributions help decide the range of lambda values to sample FLood2 across; in this case, a range of $\log_{10}(|\lambda_2|)$ = 5 - 9 was selected sampled at 20 evenly spaced intervals to resolve the behavior across thresholds.

Analyzing the relationship between the average vortex volume and λ_2 threshold in Fig. 10 indicates that increasing the Reynolds number results in a smaller average vortex size, despite the λ_2 occupying a larger fraction of the flow field at any given threshold. This behavior occurs because higher Reynolds numbers generate small vortices in regions previously devoid of turbulence at a given time, as well as fragment large vortices into multiple smaller vortices. This essentially quantitates the qualitative observations from λ_2 contour plots previously discussed and seen in Fig. 8.
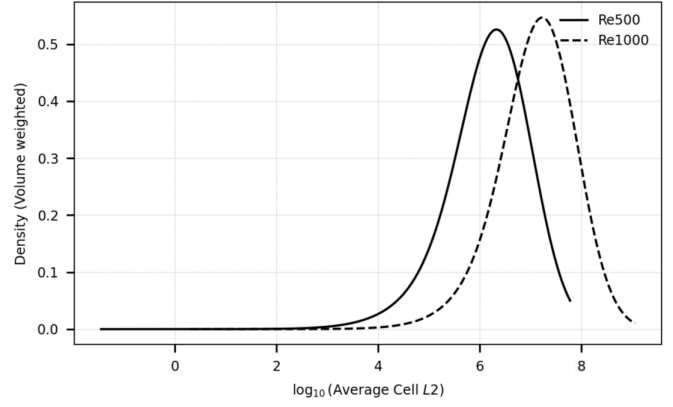

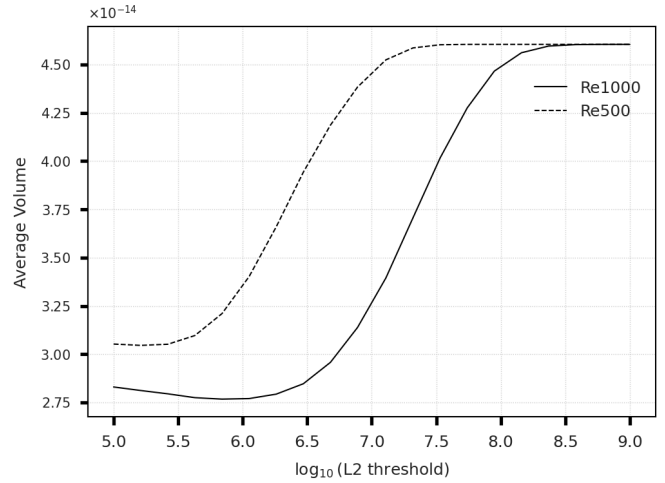Fig. 9: Volume-weighted distribution of $\log_{10}(|\lambda_2|)$ after removal of positive λ_2 values

Fig. 10: Volume-weighted distribution of $\log_{10}(|\lambda_2|)$ after removal of positive λ_2 values

Looking at the distribution of vortex volumes within a single Reynolds number rather than simply tracking the average across Reynolds numbers also provides valuable insight. In Fig. 11, the distribution of vortex volumes at Re = 500 shows a progressive shift toward larger average sizes as the λ_2 cutoff threshold increases. Although initially counterintuitive, this is consistent with the turbulent energy spectrum, where most kinetic energy comes from low frequency large-scale eddies, so by filtering for high-intensity we naturally isolate fewer, but bigger, coherent vortices. Note that the small oscillations in the histogram bars are simply artifacts of having too few samples given the bar resolution, and the quantization of island volumes on a structured hexahedral mesh since there are only a few discrete cell-volume values.
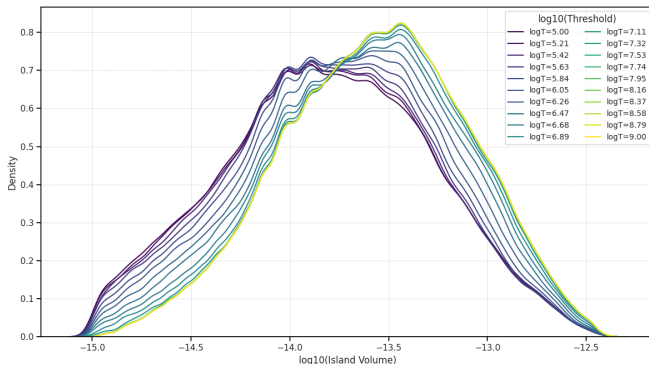
Fig. 11: Volume-weighted distribution of $\log_{10}(|\lambda_2|)$ after removal of positive λ_2 values

Increasing Reynolds number from 500 to 1000 in Fig. 12 altered the vortex size distribution by broadening and shifting it towards larger vortices at lower λ_2 thresholds. At the stricter thresholds, the distribution remained largely unchanged, suggesting that the increase in flow intensity at Re = 1000 primarily affected weaker vortices. Higher Reynolds numbers would likely further shift the distributions towards larger vortices even at stricter criteria.
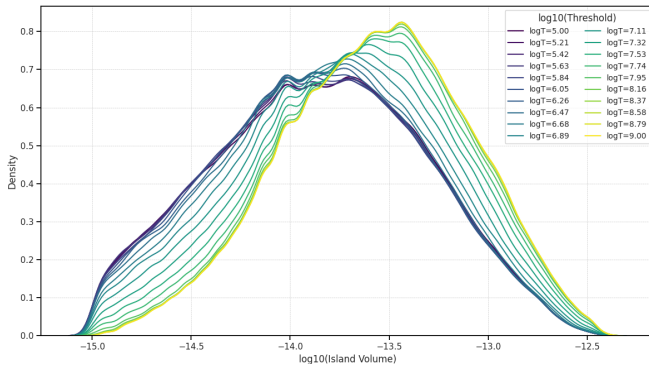

Fig. 12: Volume-weighted distribution of $\log_{10}(|\lambda_2|)$ after removal of positive λ_2 values

VI. Conclusion

This study originally aimed to characterize turbulence in a helical coil using the newly developed FLood2 algorithm, however, the simulations performed produced laminar flow conditions and contained no turbulence, making quantitative vortex analysis impossible.

To validate FLood2, it was instead applied to an SZ pipe in a fully turbulent regime, where it successfully identified coherent vortical structures, extracted quantitative metrics, and enabled objective comparison of flow fields.

The next steps involve conducting helical coil simulations at higher Reynolds numbers, and applying the FLood2 algorithm on the resulting flow fields. Next, although vortex location data was not analyzed in this study, collapsing symmetrical geometries along their axis of symmetry to generate vortex-density contours as a function of λ_2 thresholds could yield interesting results, as one could see how vortices shift in the domain across flows and strength criteria.

To conclude, the FLood2 algorithm extends the Lambda 2 method and provides valuable quantitative insight that aligns with traditional turbulence-characterization techniques.

VII. Statement of Contributions

Samuel Harrison (S.H.), Frédéric Morin (F.M.), Jan Haelssig (J.H.), Arturo Macchi (A.M.)

The conception, development, verification, and application of the presented idea were completed by S.H. Review of the manuscript, interpretation of results, and simulation workflow debugging was aided by F.M., who also provided data for the SZ geometry. J.H. and A.M. supervised the project.

References

[1] D. Prabhanjan, G. Raghavan, T. Rennie, *International Communications in Heat and Mass Transfer* **2002**, *29*, 185.
[2] A. N. Dravid, K. A. Smith, E. W. Merrill, P. L. T. Brian, *AIChE Journal* **1971**, *17*, 1114.
[3] R. Gupta, R. K. Wanchoo, T. R. M. Jafar Ali, *Industrial & Engineering Chemistry Research* **2011**, *50*, 1150.
[4] I. Di Piazza, M. Ciofalo, *International Journal of Thermal Sciences* **2010**, *49*, 653.
[5] J. S. Jayakumar, S. M. Mahajani, J. C. Mandal, K. N. Iyer, P. K. Vijayan, *Computers & Chemical Engineering* **2010**, *34*, 430.
[6] P. M. Ligrani, A Study of Dean Vortex Development and Structure in a Curved Rectangular Channel with Aspect Ratio of 40 at Dean Numbers up to 430, **1994**.
[7] I. Di Piazza, M. Ciofalo, *International Journal of Thermal Sciences* **2010**, *49*, 653.
[8] A. Sheeba, C. M. Abhijith, M. Jose Prakash, *International Journal of Refrigeration* **2019**, *99*, 490.
[9] S. Klingl, S. Lecheler, M. Pfitzner, *European Journal of Mechanics - B/Fluids* **2024**, *105*, 119.
[10] J. Jeong, F. Hussain, *Journal of Fluid Mechanics* **1995**, *285*, 69.
[11] Y. Dong, Y. Yan, C. Liu, *Applied Mathematical Modelling* **2016**, *40*, 500.
[12] S. Stegmaier, U. Rist, T. Ertl, "Opening the can of worms: An exploration tool for vortical flows," **2005**.
[13] W.-H. Chen, R. Jan, *Journal of Fluid Mechanics* **1992**, *244*, 241.
[14] Torsion Effect on Fully Developed Flow in a Helical Pipe | Journal of Fluid Mechanics | Cambridge Core.
[15] D. G. Xie, *International Journal of Heat and Fluid Flow* **1990**, *11*, 114.
[16] Z. Jinsuo, Z. Benzhao, *Acta Mechanica Sinica* **1999**, *15*, 299.
[17] C. Geuzaine, J.-F. Remacle, *International Journal for Numerical Methods in Engineering* **2009**, *79*, 1309.
[18] C. Prudhomme, "An Introduction to the Finite Element Method with Comsol Multiphysics," **2016**, pp. 35.
[19] The p and H-p Versions of the Finite Element Method, Basic Principles and Properties | SIAM Review.
[20] D. Moxey, C. D. Cantwell, Y. Bao, A. Cassinelli, G. Castiglioni, S. Chun, E. Juda, E. Kazemi, K. Lackhove, J. Marcon, G. Mengaldo, D. Serson, M. Turner, H. Xu, J. Peiró, R. M. Kirby, S. J. Sherwin, *Computer Physics Communications* **2020**, *249*, 107110.
[21] R. C. Moura, A. Cassinelli, A. F. C. da Silva, E. Burman, S. J. Sherwin, *Computer Methods in Applied Mechanics and Engineering* **2022**, *388*, 114200.
[22] H. Xu, C. D. Cantwell, C. Monteserin, C. Eskilsson, A. P. Engsig-Karup, S. J. Sherwin, *Journal of Hydrodynamics* **2018**, *30*, 1.
[23] R. Kirby, G. Karniadakis, *Journal of Computational Physics* **2003**, *191*, 249.
[24] G. Mengaldo, D. De Grazia, D. Moxey, P. Vincent, S. Sherwin, *Journal of Computational Physics* **2015**, *299*, 56.
[25] G. Karniadakis, S. Sherwin, "Spectral/HP Element Methods for Computational Fluid Dynamics," **2005**, p.
[26] V. Kolář, *International Journal of Heat and Fluid Flow* **2007**, *28*, 638.
[27] S. Kida, H. Miura, *European Journal of Mechanics - B/Fluids* **1998**, *17*, 471.

[28]   A. Cioncolini, L. Santini, *Experimental Thermal and Fluid Science*
       2006, *30*, 367.